

ANISOTROPIC CHEMICAL ETCHING OF III–V CRYSTALS

DISSOLUTION SLOWNESS SURFACE AND APPLICATION TO GaAs

C. R. TELLIER*, G. HUVE and T. G. LEBLOIS

*Laboratoire de Chronométrie Electronique et Piézoélectricité, E.N.S.M.M.,
26 chemin de l'épitaphe, 25030 Besançon Cedex, France*

(Received 2 June 2003; In final form 28 July 2003)

The analytical equation for the dissolution slowness surface of III–V crystals that belong to point group $\bar{4}3m$ is derived using a tensorial analysis of the anisotropic chemical dissolution. The role played by orientation functions in the generation of the dissolution slowness extrema is discussed. Four different databases composed of dissolution constants are proposed. The final shape of cross-sectional dissolution profiles etched in differently oriented GaAs surfaces is analyzed and compared with published experimental results. Finally etching shapes of micromachined membranes and mesa are derived showing that the anisotropy for the GaAs crystal is probably of type 2 rather than of type 1.

Keywords: GaAs; Anisotropic etching; Tensorial and kinematic model; TENSOSIM

1 INTRODUCTION

In the last few decades, semi-conducting GaAs has been studied because it is one of the III–V crystals widely used for electronic and optical devices. Moreover, on one hand, semi-conducting type P GaAs possesses a high shear piezoresistance coefficient π_{44} [1] and on the other hand, semi-insulating GaAs shows interesting piezoelectric properties [2]. So in the past few years applications of piezoresistive and piezoelectric effects in GaAs have been investigated to design new mechanical sensors [2–6]. The reason for this interest is the possibility of fabricating micro-mechanical devices in GaAs wafers by micromachining. Effectively several studies [7–14] have shown that the chemical etching of GaAs in various etchants is anisotropic. In the micromachining of mechanical devices the anisotropy provides reproducible shapes because structures are often limited by crystallographic planes. It is in particular the case of silicon for which the micromachining technology prevails for industrial applications. Previously published results [7–9, 13] on the anisotropic etching of GaAs

* Corresponding author. E-mail: ctellier@ens2m.fr

plates indicate that grooves micromachined in (001) , $\{110\}$ and $\{111\}$ plates are bounded by crystallographic planes. However, the GaAs crystal has a noncentrosymmetric structure, and consequently one can reasonably expect that grooves with different dissolution profiles will be formed on the two sides of $(hk0)$ and (hhl) plates. Shaw [7] and Takebe *et al.* [9] report that grooves micromachined along orthogonal $\langle 110 \rangle$ directions on (001) , (110) , $(\bar{1}\bar{1}\bar{1})B$ and $(111)A$ wafers exhibit effectively different cross-sectional shapes. However, to our knowledge, there is a lack of information for structures micromachined on others $(hk0)$ and (hhl) GaAs plates even if these orientations have potential advantages for some piezoelectric and piezoresistive applications.

The anisotropic etching of crystals can be conveniently described by kinematic models. These models offer the possibility of prediction for etching shapes [9, 13] specially by using Wulff type constructions [7]. Among these models the kinematic and tensorial model (KT model) proposed several years ago by Tellier [15–16] has the advantage of allowing us to derive etching shapes by numerical simulations [17–20]. The aim of this paper is, in the first step, to develop calculations to express the analytical equation for the dissolution slowness surface of III–V crystals belonging to the $\bar{4}3m$ crystallographic class and to outline the role played by orientation functions. Secondly, several sets of dissolution constants are used to generate (110) polar plots of the dissolution slowness that agree with previously published results. In particular theoretical cross-sectional shapes for grooves are derived from proposed dissolution slowness surfaces and compared with experimental shapes. Finally, theoretical investigations were made in order to provide additional information on the micromachining of GaAs surfaces.

2 DISSOLUTION CONSTANTS AND DISSOLUTION SLOWNESS SURFACE

2.1 Theoretical Framework of the KT Model

The KT model is a 3D model [15] directly derived from the Frank's model [21]. As other kinematic models [13, 15, 22] the aim of the model is to calculate the displacement \mathbf{P} of a moving surface element $\Delta\mathbf{S}$ of any orientation within the crystal during the dissolution. As suggested by Frank and co-workers [21], Tellier introduces a dissolution slowness vector \mathbf{L} to characterize the anisotropy of the chemical attack. This vector is related to a physical measurable quantity, namely the etch rate of a crystallographic plane. Let us recall that the dissolution slowness vector \mathbf{L} is defined in such a way that its magnitude L is the reciprocal of the etch rate and its direction coincides with that of the unit inward normal \mathbf{n} to the surface element. It is clear that when the orientation of the surface element varies, the vector \mathbf{L} generates in space a representative surface named the dissolution slowness surface. At this point it should be remarked that the displacement vector \mathbf{P} of a moving surface element can be determined if the dissolution slowness surface is known [15]. The major advantage of the KT model is to propose an analytical equation for the dissolution slowness surface from which Cartesian components of displacement vectors can be calculated. Tellier adopted a tensorial method to express the dependence $L(\varphi, \theta)$ of the magnitude of the dissolution slowness vector on orientation. If we adopt the convention referred to in Ref. [23] the orientation of a surface element corresponding to a doubly rotated plate is defined by two angles of cut φ and θ in such a way that the Cartesian components of the unit vector \mathbf{n} in the reference system (crystallographic axes) are given by

$$n_1 = \sin \varphi \cos \theta, \quad n_2 = -\cos \varphi \cos \theta, \quad n_3 = -\sin \theta. \quad (1)$$

Consequently the orientation dependence of $L(\varphi, \theta)$ can be conveniently replaced by a dependence on n_1, n_2 and n_3 . Tellier [15–17] suggested that the equation for the dissolution slowness $L(n_1, n_2, n_3)$ can be written as a polynomial regression involving the Cartesian components of \mathbf{n} . So we have an equation

$$L(n_1, n_2, n_3) = D_o + D_i n_i + D_{ij} n_i n_j + D_{ijk} n_i n_j n_k + D_{ijkl} n_i n_j n_k n_l + \dots \quad (2)$$

in which the dissolution constants $D_i, D_{ij}, D_{ijk}, \dots$ are components of dissolution tensors of increasing ranks. The number of dissolution constants for a tensor of given rank N_R is reduced in two ways:

- (i) Firstly, we cannot distinguish products of Cartesian components obtained by permutations so we assume that dissolution constants corresponding to permutations of subscripts are equal.
- (ii) Secondly, the number of dissolution constants is reduced by the symmetry of the crystal. So we are sure that the analytical equation for the dissolution slowness surface will reflect all the symmetry of the crystal.

To determine the independent dissolution constants for the crystallographic class $\bar{4}3m$ we adopt a procedure that is described in the following section.

2.2 The Independent Dissolution Constants

First of all let us recall that the majority of III–V crystals (GaAs, GaP, InSb, ...) belong to the $\bar{4}3m$ crystallographic class of the cubic system. The Cartesian references axes (x_1, x_2, x_3) coincide with the $\langle 100 \rangle$ directions. Moreover the zincblende structure possesses three inverse four-fold axes that correspond to $\langle 100 \rangle$ directions. It should also be noticed that for all classes of the cubic system a cyclic permutation of indices leaves the atomic arrangement unchanged, that is to say, leaves components of tensors unchanged.

Let us now consider a transformation from references axes (x_1, x_2, x_3) to primed axes (x'_1, x'_2, x'_3) in which the dissolution constants are changed into primed dissolution constants. It is clear that if the transformation is a symmetry transformation associated with point group $\bar{4}3m$, primed dissolution constants must be equal to corresponding reference constants. Dissolution constants that do not verify this condition must vanish.

At this point it is of interest to recall that dissolution constants transform as do the products of corresponding coordinates. For the point group $\bar{4}3m$ and for a symmetry transformation associated with $\bar{4}$ axes the coordinates transform as follows:

$$\bar{4} \text{ axis } x_1: \quad x'_1 = -x_1, \quad x'_2 = -x_3, \quad x'_3 = x_2 \quad (3)$$

$$\bar{4} \text{ axis } x_2: \quad x'_1 = x_3, \quad x'_2 = -x_2, \quad x'_3 = -x_1 \quad (4)$$

$$\bar{4} \text{ axis } x_3: \quad x'_1 = -x_2, \quad x'_2 = x_1, \quad x'_3 = -x_3 \quad (5)$$

so e.g. for a tensor of rank 7 according to Eq. 1 we have

$$D'_{1112222} = D_{1112222} \rightarrow -D_{1113333} \quad \text{since } x_1^3 x_2^4 \rightarrow -x_1^3 x_3^4$$

and

$$D'_{1113333} = D_{1113333} \rightarrow D_{1112222} \quad \text{since } x_1^3 x_3^4 \rightarrow x_1^3 x_2^4$$

From these relations we can conclude that $D_{1112222}$ and $D_{1113333}$ vanish. In fact examination of Eqns. (3)–(5) indicates that for tensors of even rank the remaining dissolution constants are

those corresponding to combinations of even numbers of subscripts 1 and/or 2 and/or 3. For tensors of odd rank the independent dissolution constants are those that possess odd numbers of subscripts 1–3. Further we take into account that a cyclic permutation of subscripts does not modify the physical properties. For example, for a tensor of rank 7 we obtain the two following complementary relations between dissolution constants

$$D_{1233333} = D_{1222223} = D_{1111123}, \quad D_{1222333} = D_{1112333} = D_{1112223}.$$

Applying this procedure for dissolution tensors of rank N_R up to 12 we obtain the non-vanishing dissolution constants listed in Table I. For convenience in this table we adopt for tensors of rank $N_R > 5$ the following notation for the subscripts

$$i(N_i)j(N_j)k(N_k)$$

where N_i , N_j , and N_k are the number of subscripts i , j and k , respectively.

TABLE I Independent Dissolution Constants for Tensors of Rank N_R .

N_R	Independent dissolution constants	N_D
0	D_o	1
1	–	–
2	D_{ii} (D_{11})	1
3	D_{123}	6
4	D_{iii} (D_{1111})	1
	D_{ijj} (D_{1122})	6
5	D_{iijk} (D_{11123})	20
6	$D_{i(6)}$ ($D_{1(6)}$)	1
	$D_{i(4)j(2)}$ ($D_{1(4)2(2)}$)	15
	$D_{i(2)j(2)k(2)}$ ($D_{1(2)2(2)3(2)}$)	90
7	$D_{i(5)j(1)k(1)}$ ($D_{1(5)2(1)3(1)}$)	42
	$D_{i(3)j(3)k(1)}$ ($D_{1(3)2(3)3(1)}$)	140
8	$D_{i(8)}$ ($D_{1(8)}$)	1
	$D_{i(6)j(2)}$ ($D_{1(6)2(2)}$)	28
	$D_{i(4)j(4)}$ ($D_{1(4)2(4)}$)	70
	$D_{i(4)j(2)k(2)}$ ($D_{1(4)2(2)3(2)}$)	420
9	$D_{i(7)j(1)k(1)}$ ($D_{1(7)2(1)3(1)}$)	72
	$D_{i(5)j(3)k(1)}$ ($D_{1(5)2(3)3(1)}$)	504
	$D_{i(3)j(3)k(3)}$ ($D_{1(3)2(3)3(3)}$)	1680
10	$D_{i(10)}$ ($D_{1(10)}$)	1
	$D_{i(8)j(2)}$ ($D_{1(8)2(2)}$)	45
	$D_{i(6)j(4)}$ ($D_{1(6)2(4)}$)	210
	$D_{i(6)j(2)k(2)}$ ($D_{1(6)2(2)3(2)}$)	1260
	$D_{i(4)j(4)k(2)}$ ($D_{1(4)2(4)3(2)}$)	3150
11	$D_{i(9)j(1)k(1)}$ ($D_{1(9)2(1)3(1)}$)	110
	$D_{i(7)j(3)k(1)}$ ($D_{1(7)2(3)3(1)}$)	1320
	$D_{i(5)j(5)k(1)}$ ($D_{1(5)2(5)3(1)}$)	2772
	$D_{i(5)j(3)k(3)}$ ($D_{1(5)2(3)3(3)}$)	9240
12	$D_{i(12)}$ ($D_{1(12)}$)	1
	$D_{i(10)j(2)}$ ($D_{1(10)2(2)}$)	66
	$D_{i(8)j(4)}$ ($D_{1(8)2(4)}$)	495
	$D_{i(6)j(6)}$ ($D_{1(6)2(6)}$)	924
	$D_{i(8)j(2)k(2)}$ ($D_{1(8)2(2)3(2)}$)	2970
	$D_{i(6)j(4)k(2)}$ ($D_{1(6)2(4)3(2)}$)	13860
	$D_{i(4)j(4)k(4)}$ ($D_{1(4)2(4)3(4)}$)	34650

Note: N_D is the number of dissolution constants as obtained by permutations of subscripts i , j and k . The dissolution constants that are retained to express the analytical Eq. (7) are indicated in parentheses.

2.3 The Equation for the Dissolution Slowness Surface and the Orientation Functions

At this point it is necessary to recall that according to the first procedure of reduction [reduction (i), Sec. 2.1] an independent dissolution constant for a tensor of rank N_R appears N_D times in the equation for the dissolution slowness in such a way that

$$N_D = \frac{N_R!}{N_i!N_j!N_k!}. \quad (6)$$

So accounting for Table I and relation (6) we obtain the following equation for the dissolution slowness surface

$$\begin{aligned} L(n_1, n_2, n_3) = & D_o + D_{11}H_1 + 6D_{123}G_1 + D_{1111}H_2 + 6D_{1122}K_1 + 20D_{11223}G_1H_1 \\ & + D_{1(6)}H_3 + 15D_{1(4)2(2)}(H_2 - H_3) + 90D_{1(2)2(2)3(2)}G_2 \\ & + 42D_{1(5)2(1)3(1)}G_1H_2 + 140D_{1(3)2(3)1(1)}G_1K_1 + D_{1(8)}H_4 \\ & + 28D_{1(6)2(2)}(H_3 - H_4) + 70D_{1(4)2(4)}K_2 + 420D_{1(4)2(2)3(2)}G_2H_1 \\ & + 8D_{1(7)2(1)3(1)}G_1H_3 + 8D_{1(5)2(3)3(1)}G_1(H_2 - H_3) + 8D_{1(3)2(3)3(3)}G_3 \\ & + D_{1(10)}H_5 + 45D_{1(8)2(2)}(H_4 - H_5) + 210D_{1(6)2(4)}(K_2 - G_2K_1) \\ & + 1260D_{1(6)2(2)3(2)}G_2H_2 + 3150D_{1(4)2(4)3(2)}G_2K_1 + 110D_{1(9)2(1)3(1)}G_1H_4 \\ & + 1320D_{1(7)2(3)3(1)}G_1(H_3 - H_4) + 9240D_{1(5)2(3)3(3)}G_3 \\ & + 2772D_{1(5)2(5)3(1)}G_1K_2 + D_{1(12)}H_6 + 66D_{1(10)2(2)}G_2(H_2 - H_3) \\ & + 495D_{1(8)2(4)}(K_2 - 2K_1K_2 - 3G_4) + 1848D_{1(6)2(6)}K_3 \\ & + 2970D_{1(8)2(2)3(2)}G_2H_3 + 13860D_{1(6)2(4)3(2)}G_2(H_2 - H_3) \\ & + 34650D_{1(4)2(4)3(4)}G_4 \end{aligned} \quad (7)$$

where we introduce the orientation functions G_g , H_h and K_k that are defined by relations:

$$G_g = (n_1n_2n_3)^g \quad (8)$$

$$H_h = n_1^{2h} + n_2^{2h} + n_3^{2h} \quad (9)$$

$$K_k = (n_1n_2)^{2k} + (n_1n_3)^{2k} + (n_2n_3)^{2k}. \quad (10)$$

In view of Eq. (9) it is obvious that $H_1 = 1$. So in Eq. (7) for tensors of rank $N_R > 8$ this term is replaced by unity in order to simplify the final expression.

Let us recall that the Cartesian components of the unit inward normal \mathbf{n} to a surface element with angles of cut (φ, θ) are given by Eq. (1). Hence functions H_h and K_k are even functions of angles of cut φ and θ . Changes of 180° in the angles of cut leave the dissolution slowness L unchanged. This behavior is also met by the function G_g when g takes even values. Moreover only dissolution constants related to H_h and K_k determine the dissolution slowness of $\{hk0\}$ plates ($\varphi = \varphi_o$, $\theta = 0^\circ$). So the two faces of $\{hk0\}$ GaAs plates etch with the same rate. In contrast the dissolution slowness L of $\{hhl\}$ surfaces [$\varphi = -45^\circ$, $\theta = \theta_o$ for an (hhl) surface] involves dissolution constants associated with G_g functions. Consequently the two faces of $\{hhl\}$ plates must have different dissolution slownesses. Thus the experimental determination of dissolution constants from an analysis of experimental shapes will be more complicated for GaAs than for Si. Therefore it seems of interest to follow the evolution in the polar graphs of functions G_g , H_h and K_k with the polar angle Ψ . Values Ψ_{\min} and Ψ_{\max} of the polar angle corresponding to minima and maxima in polar graphs, respectively, are thus determined. Effectively let us recall that the (010) polar graph illustrates changes in the dissolution slowness $L_{\{hk0\}}$ of $\{hk0\}$ surfaces

while the (1 1 0) polar graph gives dissolution slownesses $L_{\{hhl\}}$. So consider φ_e and θ_e to be values of angles of cut corresponding to extrema ($e = \min$ for minima, $e = \max$ for maxima) in (0 1 0) and (1 1 0) polar graphs of orientation functions, respectively. It is clear that we can extract values of φ_e (for $\{hk0\}$ surfaces) and of θ_e (for $\{hhl\}$ surfaces) from (0 0 1) and (0 1 1) polar graphs, respectively.

Figures 1–3 give polar plots of orientation functions in (0 1 0), in (1 1 0) and in some (h h l) planes including the (1 1 1) plane. As the purpose of this study is to determine angles related to extrema for some orientation functions we give magnified representations of polar plots. Moreover Figure 4 shows polar graphs related to some combinations of orientation functions appearing in Eq. (7). From a careful examination of these graphs some essential features are typified:

- (i) The (0 1 0) polar graphs related to H_h and K_k functions give effectively similar values when the polar angle is changed from φ to $\varphi + 180^\circ$ in accordance with the preceding remark.
- (ii) A similar behavior is observed for (1 1 0) polar graphs related to H_h and K_k when the polar angle is changed from θ to $\theta + 180^\circ$.
- (iii) If we consider the cross-sectional planes (1 0 0) and (1 1 0) we observe that angles for which polar plots of H_h pass through extrema remain unchanged when we work with dissolution tensors with increasing rank N_R (see *e.g.* Fig. 2).
- (iv) If we examine $\{1\ 1\ 0\}$ polar graphs related to G_1 , G_2 and G_3 in Figure 1 and if we now consider absolute values of G_i we obtain similar values for angles Ψ_e whatever the value of subscript g . Only $\{h\ h\ l\}$ polar diagrams show a more complex evolution with N_R .
- (v) In the case of K_k functions the nature of an extremum generated for a given angle Ψ_e is inverted when the subscript k takes successively odd and even values [compare (1 1 0) graphs related to K_1 and K_2 in Fig. 3].

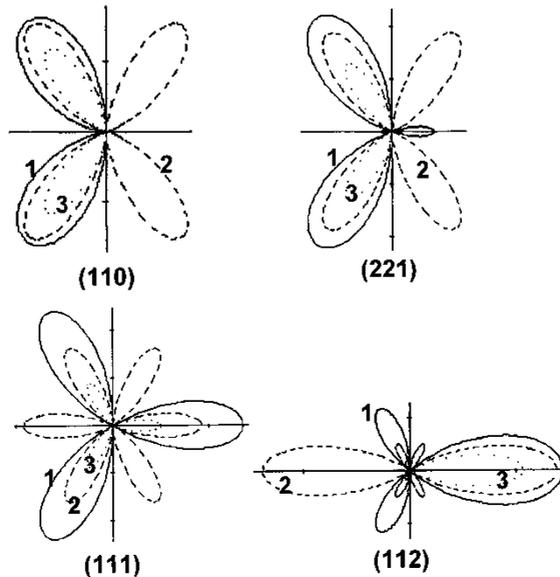


FIGURE 1 Polar plots (in arbitrary units) of functions G_1 (full lines), G_2 (broken lines) and G_3 (dotted lines) in various cross-sectional planes as indicated in figures. The factor of amplification for functions G_2 and G_3 with respect to function K_1 is equal to 5 and 20, respectively.

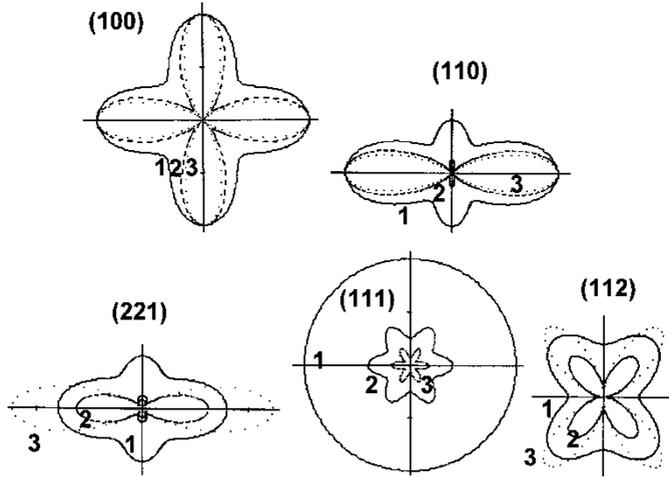


FIGURE 2 Polar plots (in arbitrary units) of functions H_2 (full lines), H_4 (broken lines) and H_6 (dotted lines) in various cross-sectional planes as indicated in figures. The factor of amplification for functions H_6 with respect to function H_2 (or to function H_4) was adjusted to 2.5 for (112) and (221) cross-sections in order to distinguish more easily the secondary extrema in the H_6 polar plot.

Taking into account these observations for polar angles Ψ_e corresponding to extrema in (001), (110) and (111) polar graphs of G_g , H_h and K_k functions are shown in Table II. This table reveals several interesting features:

- (i) In the (001) cross-sectional plane the orientation functions H_h and K_k exhibit extrema for angles corresponding to $\{100\}$ and $\{110\}$ crystallographic planes independently of the tensor rank N_R . However, although minima and maxima occur for $\{110\}$ and $\{100\}$ planes in the case of H_h functions we observe that the role of $\{100\}$ and $\{110\}$ planes are interchanged for K_k functions. Moreover, using the combined orientation functions does not introduce new values for angles associated with extrema.
- (ii) Polar plots of H_h functions lying in the (110) plane present extrema associated with either $\{111\}$ surfaces ($\Psi = 55^\circ$ or 125°) or $\{100\}$ and $\{110\}$ surfaces ($\Psi = 0^\circ, 90^\circ$ or 180°). These orientations also play a major role when we are concerned with extrema related to K_k or G_g functions. However, for tensors of higher rank function K_3 and some combined functions show extrema for angles Ψ_e that correspond to surfaces other than $\{100\}$, $\{110\}$ and $\{111\}$. In fact the values are close to values associated with the $\{554\}$ or $\{112\}$ surfaces.
- (iii) If we turn our attention to (111) polar graphs and to extrema of a given type (minimum or maximum) we observe that in most cases extrema in H_h and K_k orientation functions appear for the following sets of values ($\Psi_e = 0^\circ, 60^\circ, 120^\circ, 180^\circ$ or $\Psi_e = 30^\circ, 90^\circ, 150^\circ$) with a change in the extremum type sometimes when we look at G_g and K_k . These sets of values remain valid for functions G_2 and G_4 that are involved in tensors of even rank. Values of Ψ_e extracted for G_1 and G_3 polar diagrams also belong to these two sets. Thus $\{110\}$ and $\{112\}$ surfaces seem to be associated with extrema in $\{111\}$ polar graphs of orientation functions.

In conclusion it appears that it is not possible to adjust only one dissolution constant (related to a specific orientation function) to generate a valley or a protuberance for a specific orientation. In fact we have to modify several dissolution constants simultaneously without ignoring the fact that a change in a dissolution constant will affect several cross-sectional polar plots.

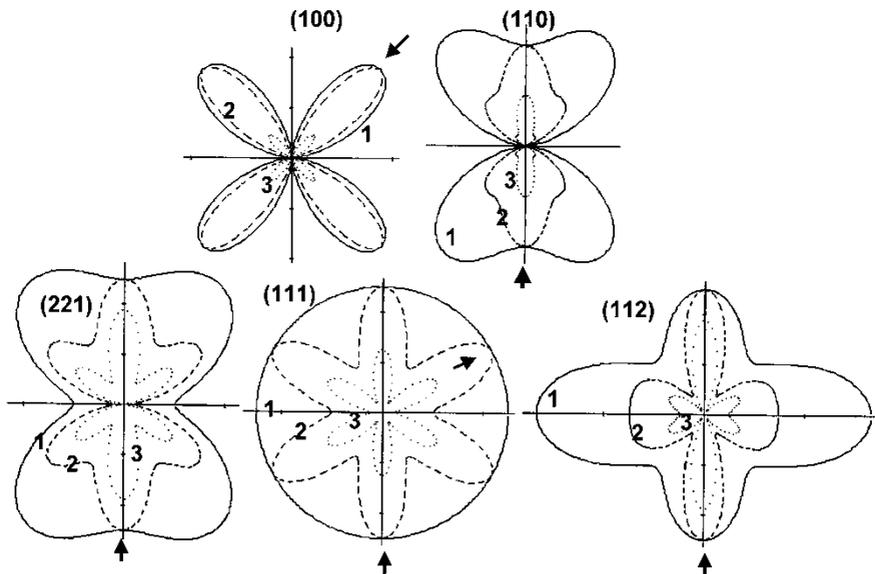


FIGURE 3 Polar plots (in arbitrary units) of functions K_1 (full lines), K_2 (broken lines) and K_3 (dotted lines) in various cross-sectional planes as indicated in figures. The factor of amplification for functions K_2 and K_3 with respect to function K_1 is equal to 4 expected for the $\{111\}$ cross-section. Arrows indicate $\langle 110 \rangle$ directions.

However, the dissolution constants related to G_g functions or to combined (G_g, H_h) functions will play a major role in the apparition of protuberances and valleys corresponding to $\{111\}$ surfaces. Different dissolution slowness surfaces are proposed in the following section and are discussed in terms of results previously reported in the literature [7–9].

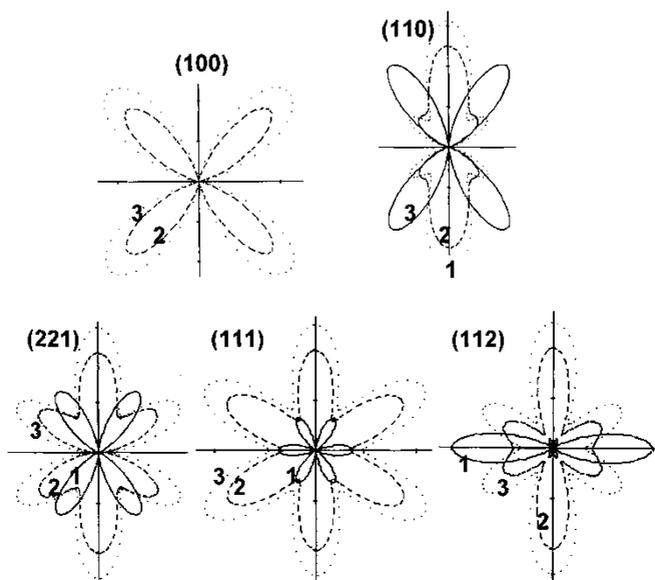


FIGURE 4 Polar plots (in arbitrary units) of G_2K_1 (full lines), $K_2-2K_1K_2$ (broken lines) and $K_2-2G_2K_1-3G_4$ (dotted lines) in various cross-sectional planes as indicated in figures. The factor of reduction for combined functions $K_2-2K_1K_2$ and $K_2-2G_2K_1-3G_4$ with respect to function G_2K_1 is equal to 0.2 and 0.5, respectively.

TABLE II Values of Alignment Angle ψ for which the Polar Plots of Orientation Functions Pass Through Minima and Maxima.

Orientation functions	(001) plane minima	(001) plane maxima	(110) plane minima	(110) plane maxima	(111) plane minima	(111) plane maxima
H_2	45°, 135°	0°, 90°, 180°	55°, 125°	0°, 90°, 180°	Constant	Constant
H_4	45°, 135°	0°, 90°, 180°	55°, 125°	0°, 90°, 180°	30°, 90°, 150°	0°, 60°, 120°, 180°
H_6	45°, 135°	0°, 90°, 180°	55°, 125°	0°, 90°, 180°	30°, 90°, 150°	0°, 60°, 120°, 180°
K_1	0°, 90°, 180°	45°, 135°	0°, 90°, 180°	55°, 125°	0°, 90°, 180°	52°, 128°
K_2	0°, 90°, 180°	45°, 135°	0°, 180°	90°	0°, 60°, 120°, 180°	30°, 90°, 150°
K_3	0°, 90°, 180°	45°, 135°	0°, 55°, 125°, 180°	48°, 90°, 132°	0°, 60°, 120°, 180°	30°, 90°, 150°
G_1	—	—	0°, 90°, 180°	55°, 125°	60°, 180° **	0°, 120° *
G_2	—	—	0°, 90°, 180°	55°, 125°	30°, 90°, 150°	0°, 60°, 120°, 180°
G_3	—	—	0°, 90°, 180°	55°, 125°	60°, 180° **	0°, 120° *
G_4	—	—	0°, 90°, 180°	55°, 125°	30°, 90°, 150°	0°, 60°, 120°, 180°
G_2K_1	—	—	0°, 90°, 180°	55°, 125°	30°, 90°, 150°	0°, 60°, 120°, 180°
$K_2-G_2K_1$	0°, 90°, 180°	45°, 135°	0°, 55°, 125°, 180°	46°, 90°, 134°	0°, 60°, 120°, 180°	30°, 90°, 150°
$K_2-2K_1K_2-3G_4$	0°, 90°, 180°	45°, 135°	0°, 55°, 125°, 180°	37°, 90°, 143°	0°, 60°, 120°, 180°	30°, 90°, 150°

Note: *, ** indicate opposite values of the orientation functions G_g . * and ** are given for positive and negative values, respectively.

3 APPLICATION TO THE CHEMICAL ETCHING OF GaAs CRYSTAL

3.1 Analysis of Published Results

An anisotropic chemical etching process is characterized by the formation of dissolution figures on etched surfaces or by the development of limiting facets beneath the mask in the case of localized etching. Several studies [17, 18, 24–26] have shown that shapes of dissolution figures and formation of limiting facets are directly correlated to the presence of maxima in polar graphs of L (localized etching) or of extrema in the dissolution slowness surface (dissolution figures and micromachined structures). We therefore analyze previous results in order to determine orientations corresponding to these extrema. Most of the published results are concerned with localized etching.

Shinya Iida and Kazuhiro Ito studied the anisotropic etching of GaAs in the $\text{H}_2\text{SO}_4:\text{H}_2\text{O}_2:\text{H}_2\text{O}$ system [8]. Square holes were micromachined in differently oriented GaAs plates. Etching rates of the two faces of various plates were measured showing orientation effects. Several conclusions were drawn from this study:

- (i) The $\{111\}_A$ plane has the lowest etching rate $R_{\{111\}_A}$ (*i.e.* the largest dissolution slowness).
- (ii) The anisotropy ratio $k_{\{111\}} = R_{\{111\}_B}/R_{\{111\}_A}$ depends markedly on the $\text{H}_2\text{SO}_4:\text{H}_2\text{O}_2:\text{H}_2\text{O}$ system.
- (iii) Specific etching systems such as the $8\text{H}_2\text{SO}_4:1\text{H}_2\text{O}_2:1\text{H}_2\text{O}$ system result in small changes in etch rate with orientation of $\{hh\ell\}$ surfaces.
- (iv) In the case of $\{100\}$ plates one of the two faces does not correspond to a protuberance of the dissolution slowness surface in contrast with the silicon crystal behavior [13, 18–20, 24–26]. These authors also estimated values of intersection angles α_i that successive facets forming a cross-sectional profile (Fig. 5) make with the reference surface.

Shaw [7] studied the morphology of $\{110\}$ dissolution profiles (localized etching) etched in (001) GaAs using various $\text{H}_2\text{SO}_4:\text{H}_2\text{O}_2$ and $\text{HCl}:1\text{H}_2\text{O}_2$ etchant compositions. He concluded that the anisotropy ratio $k_{\{111\}}$ and final shape of dissolution profiles varied systematically with the etchant composition. In particular the anisotropy ratio was found to take values in the range 4.2–1.5. Moreover, Shaw proposed approximate polar plots [lying in the (110) section] for the etching rate of $\{hh\ell\}$ planes from which predicted dissolution profiles were geometrically constructed. He showed that whatever $k_{\{111\}}$ (011) is cross-sectional localized dissolution profiles are re-entrant profiles (Fig. 5) in accordance with previous published results [8, 9]. However, it was clearly demonstrated that the extent of limiting facets that participate to the (110) dissolution profile depends on the anisotropy ratio. In fact for the

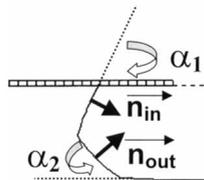


FIGURE 5 A schematic representation of a re-entrant profile, similar to those proposed by Shaw [7], that is composed of a facet with an inward normal n_{in} and a facet with an outward normal n_{out} . Definition of successive intersection angles α_i .

H₂SO₄:H₂O₂: H₂O etchant facet 2 with inclination α_2 (Fig. 5) tends to disappear with increasing $k_{\{111\}}$. Moreover some etchants cause the formation of curved profiles.

More recently Takebe *et al.* [9] investigated the chemical etching of (001), {110}, {111}A and {111}B surfaces in HF:H₂O₂:H₂O mixtures. For these surfaces changes in the etch rate with system composition were studied, showing that except for a system with high H₂O and with low H₂O₂ concentrations the {111}B surface dissolves more rapidly than the {111}A surface when the anisotropy ratio $k_{\{111\}}$ varies from about 3.8 to about 0.9. They also controlled values of successive intersection angles α_i and connected these angles with main limiting {hhℓ} facets. Here again elements associated with the {111}A planes were found to be less curved than elements connected with the {111}B planes.

3.2 Dissolution Slowness Surfaces for GaAs and Theoretical Etching Shapes

Taking into account the main features summarized in Section 3.1 we retain four different databases (sets of dissolution constants) that give (Tab. III) values in the range 4.2–1.7 for the anisotropy ratio $k_{\{111\}} = L_{\{111\}A} / L_{\{111\}B}$. Figures 6 and 7 illustrate a change in the polar plots of **L** with orientation for the laws 1–4. In order to make a comparison with Shaw's results [7] more simple, the (110) polar diagrams of the etching rate are drawn in Figure 8. The reader can see that (100) polar diagrams for laws 1 and 2 differ even if anisotropy ratios are close together. Moreover (100) polar diagrams are similar for laws 1 and 4 but modifications in the dissolution constants are performed in order to increase the anisotropy ratio from 1.87 (law 1) to 4.13 (law 4). In this condition (110) polar diagrams become markedly different.

Turning our attention to Figure 8 it appears that {111}A planes are associated with minima in the etch rate (*i.e.* with maxima in *L*) for the four laws investigated here. Depending on the anisotropy ratio $k_{\{111\}}$ the etch rate of {111}B planes corresponds either to a maximum in the etch rate diagram (laws 1 and 4) or to a minimum (laws 2 and 3). Values of polar angles associated with minima and maxima in the {100} and {110} polar diagrams for *L* are listed in Table IV. Figures 6–8 and Table IV show the following:

- (i) It is possible to generate a limited number of extrema in the {110} polar diagrams that in fact are correlated to {100} and {111} crystallographic planes even if we generate more complex {100} polar graphs that contain four extrema in the angular sector (0°, 45°) (see figures related to laws 1 and 4). However, the converse situation [*i.e.*, more complex shape for the {110} polar graph than for the {100} polar graph] is easier to meet.
- (ii) Observing the changes in {110} polar diagrams of $R_{\{hh\ell\}}$ in the vicinity of (001) directions, it appears that for the four databases the etching rate passes through a maximum and through a minimum for the [001] and [00 $\bar{1}$] directions, respectively, in close accordance with the figures of Shaw [7].

TABLE III Anisotropy Ratio for the Various Etching Laws.

Etching law	Anisotropy ratio $k_{\{111\}} = \frac{L_{\{111\}A}}{L_{\{111\}B}}$
Law 1	1,87
Law 2	1,75
Law 3	2,41
Law 4	4,13

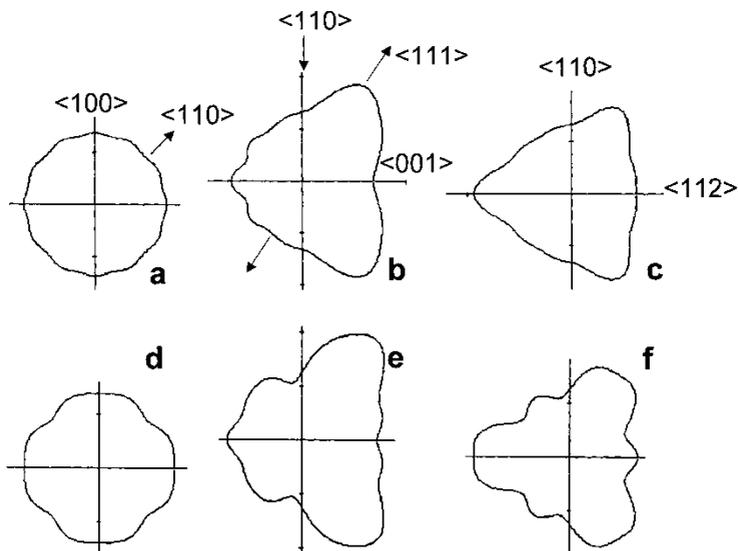


FIGURE 6 Polar plots (in arbitrary units) of the dissolution slowness in (010), (110) and (111) cross-sectional planes as derived from law 1 (a, b, c) and from law 2 (d, e, f). (a, d), (b, e) and (c, f) correspond to (010), (110) and (111) cross-sectional planes, respectively. For convenience some crystallographic directions are also indicated in these diagrams.

(iii) If we exclude law 3 the dissolution slowness of $\{100\}$ and $\{110\}$ planes are close together. Moreover for the laws considered here the dissolution slowness $L_{\{110\}}$ remains smaller than $L_{\{100\}}$. This feature does not completely satisfy the results reported by Shaw for some $\text{H}_2\text{SO}_4\text{:H}_2\text{O}_2\text{:H}_2\text{O}$ systems, but it agrees with observations made for other etching mixtures [8, 9].

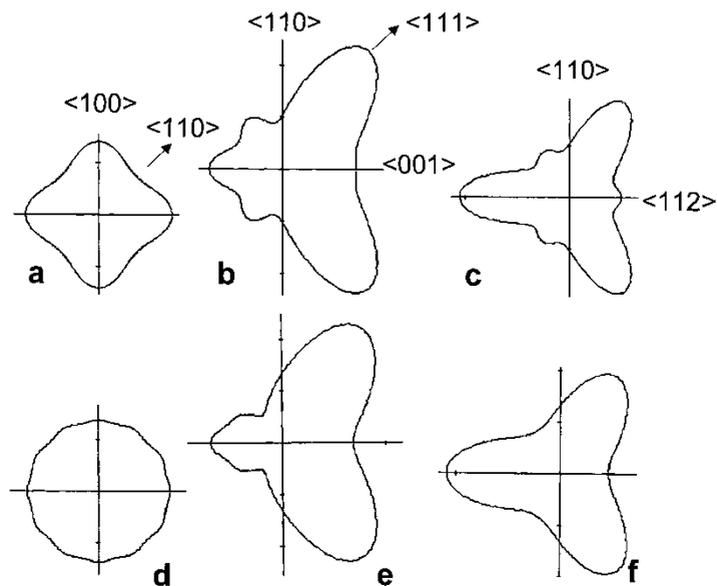


FIGURE 7 Polar plots (in arbitrary units) of the dissolution slowness in (010), (110) and (111) cross-sectional planes as derived from law 3 (a, b, c) and from law 4 (d, e, f). (a, d), (b, e) and (c, f) correspond to (010), (110) and (111) cross-sectional planes, respectively. For convenience some crystallographic directions are also indicated in these diagrams.

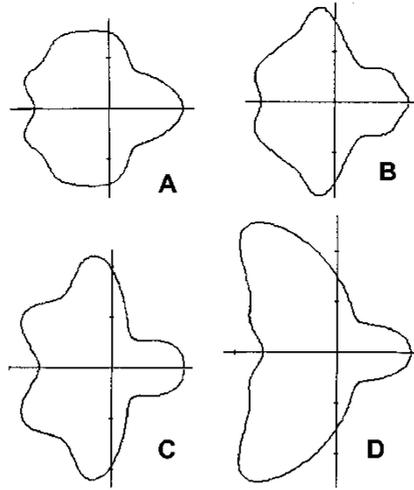


FIGURE 8 Polar plots (in arbitrary units) of the etching rate in the (1 1 0) cross-sectional plane for the four laws investigated in this paper. a, b, c and d correspond to laws 1, 2, 3 and 4, respectively.

(iv) Some extrema in polar graphs of Figures 6–8 occur for angles Ψ_c whose values differ from those listed in Table II. This is due to the introduction of more than ten dissolution constants (ranks 9–12). Effectively, combinations of dissolution constants with opposite signs and with different magnitudes allow us to generate additional extrema.

It is possible to derive etching laws that can crudely account for behaviors reported in the literature. At this point it should be remarked that generation of laws with $R_{\{100\}} > R_{\{110\}}$ can be performed by modifications of dissolution constants $D_{i(10)}$ and $D_{i(12)}$. However, the purpose of this study is to investigate the formation of limiting sidewalls in localized etchings. So slight changes in these constants that leave the nature of $L_{\{100\}}$ extrema in $\{1 1 0\}$ polar graphs unchanged has, according to dissolution criteria [27], no influence on the identification of limiting sidewalls.

3.3 Localized Etchings

In this section we investigate etching shapes of cross-sectional dissolution profiles of grooves etched on $\{1 0 0\}$, $\{1 1 0\}$ and $\{1 1 1\}$ planes and aligned along various directions D_A that make an angle Ψ_A with the rotated x'_3 axis. All theoretical shapes that constitute 2D etching

TABLE IV Values of Angles for which the (0 1 0) and (1 1 0) Cross-sectional Polar Plots of the Dissolution Slowness Pass Through Successive Extrema.

Etching law	Cross-sectional plane (0 1 0)	Cross-sectional plane (1 1 0)
Law 1	φ_{\min} : 14°, 45°, 76° φ_{\max} : 0°, 29°, 61°, 90°	ψ_{\min} : 0°, 125°, 161° ψ_{\max} : 55°, 144°, 180°
Law 2	φ_{\min} : 0°, 45°, 90° φ_{\max} : 20°, 70°	ψ_{\min} : 0°, 100°, 157° ψ_{\max} : 55°, 125°, 180°
Law 3	φ_{\min} : 0°, 90° φ_{\max} : 45°	ψ_{\min} : 0°, 100°, 148° ψ_{\max} : 55°, 125°, 180
Law 4	φ_{\min} : 14°, 45°, 76° φ_{\max} : 0°, 29°, 61°, 90°	ψ_{\min} : 125° ψ_{\max} : 55°, 180

Note: Subscripts min and max are given for the minimum and maximum, respectively.

shapes are derived from polar diagrams of \mathbf{L} using the simulator TENSOSIM. This simulator that is based on the KT model was described elsewhere [18–20, 25, 28]. In the case of the (0 1 0) plane we have chosen to derive cross-sectional profiles corresponding to $\Psi_A = \pm 45^\circ$ in order to make a direct comparison with respective (0 1 1) and (0 1 $\bar{1}$) schematic dissolution profiles proposed by Shaw [7]. For grooves micromachined on a (1 1 0) plane we studied the evolution of dissolution profiles lying in the (0 0 1) and the (1 $\bar{1}$ 0) sections *i.e.*, to study shapes of grooves aligned along the [0 0 1] direction ($\Psi_A = 0^\circ$) and along the x'_1 ($\Psi_A = -90^\circ$) axis, respectively. In this condition (1 1 0) grooves with $\Psi_A = 0^\circ$ must exhibit two sides with symmetrical dissolution profiles because {1 1 0} planes act as mirror planes. Similar values for Ψ_A are also retained for grooves etched on the two faces of a (1 1 1) wafer. So here again the two dissolution profiles derived for $\Psi_A = 0^\circ$ must satisfy the mirror symmetry associated with {1 1 0} planes. Figures 9–12 show theoretical dissolution profiles for localized etchings performed on (0 1 0), (1 1 0), (1 1 1)A and ($\bar{1}$ $\bar{1}$ $\bar{1}$)B surfaces as derived when we began with the various etching laws described in Section 3.2. In addition theoretical values of intersection angles α_i are listed in Tables V–VIII. Let us at first discuss results related to the (0 1 0) groove [Figs 9(a,b) to 11(a,b) and Tab. V]. We observe that (1 1 0) cross-sectional profiles are re-entrant profiles [Figs 9(a)–12(a)]. Until the anisotropy ratio $k_{\{111\}}$ remains smaller than 4 these profiles are composed of two elements associated with two limiting sidewalls. Moreover as the anisotropy ratio $k_{\{111\}}$ increases, the extent of facet f_2 decreases. Finally the facet f_2 disappears as $k_{\{111\}}$ reaches 4.13. Moreover (1 $\bar{1}$ 0) cross-sectional profiles are correlated to the formation of a facet with an outward normal [Figs 9(b)–12(b)] whatever the etching law. Theoretical inclinations ($\alpha_i \approx 55^\circ$, Tab. V) indicate clearly that this limiting facet is in fact a {1 1 1}A facet. These theoretical results agree well with Shaw's observations and theoretical predictions [7]. This accordance particularly concerns changes in facet f_2 with the anisotropy ratio $k_{\{111\}}$.

Let us now consider structures etched on (0 1 1) substrates [Figs 9(c,d)–12(c,d) and Tab. VI]. It appears that for the (0 0 1) cross-section we obtain as expected symmetrical dissolution

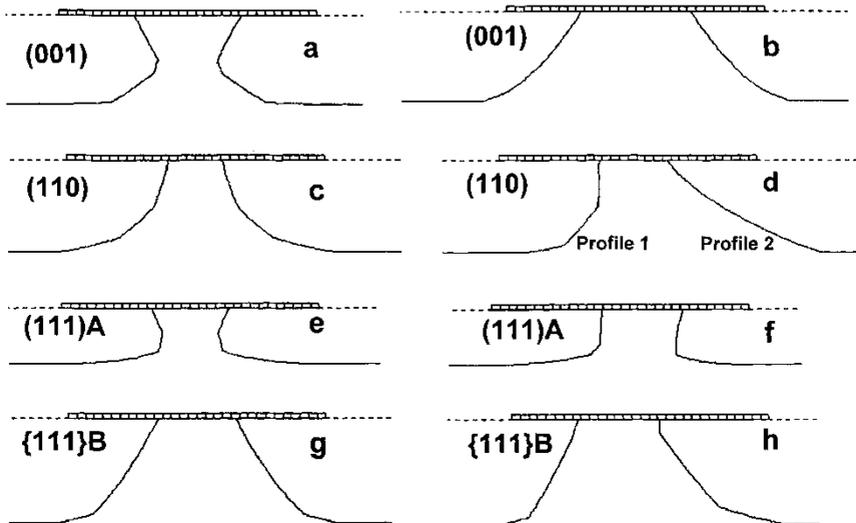


FIGURE 9 Theoretical 2D etching shapes for the cross-sections of grooves etched on surfaces indicated in the figures and aligned along specified directions defined by an angle Ψ_A . Dissolution profiles are derived from law 1. For various surfaces the angle Ψ_A takes the following values: (a) $\Psi_A = +45^\circ$, (b) $\Psi_A = -45^\circ$, (c, e, g) $\Psi_A = 0^\circ$, (d, f, h) $\Psi_A = -90^\circ$.

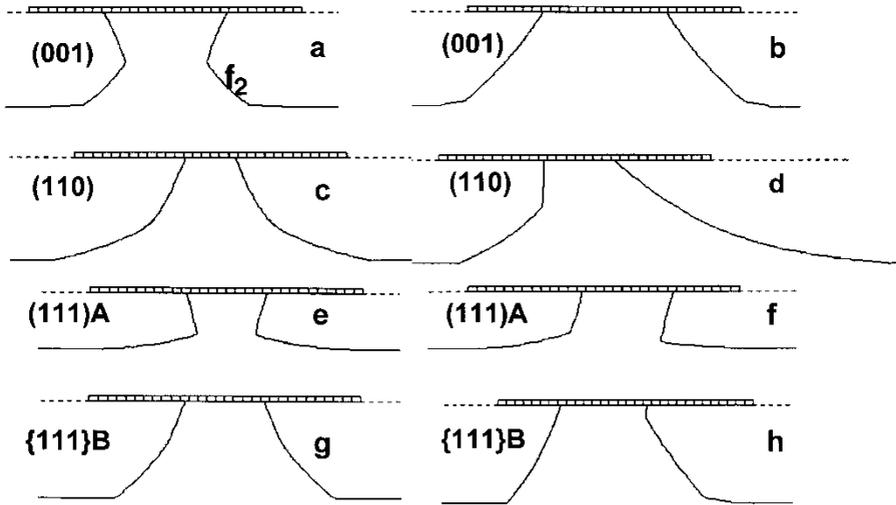


FIGURE 10 Theoretical 2D etching shapes for the cross-sections of grooves etched on surfaces indicated in the figures and aligned along specified directions defined by an angle Ψ_A . Dissolution profiles are derived from law 2. For various surfaces the angle Ψ_A takes the following values: (a) $\Psi_A = +45^\circ$, (b) $\Psi_A = -45^\circ$, (c, e, g) $\Psi_A = 0^\circ$, (d, f, h) $\Psi_A = -90^\circ$.

profiles that for law 4 investigated here contain elements with an outward normal. For laws 1 and 4 we count three linear elements because polar graphs of L (Figs 6 and 7) in the angular sector $(-90^\circ, 0^\circ)$ exhibit three maxima. The number of linear elements is reduced for profiles derived from law 2 whereas law 3 gives rise to curved profiles [Fig. 11(c)] with α_i in the range $50^\circ-30^\circ$ due to the presence of a relatively smooth maximum associated with a $\{100\}$ plane on the (001) polar graph of L . It should be pointed out that very different values for intersection angles were reported in the literature [8, 9], and so for (001) cross-sectional profiles it is difficult to make a significant comparison between theoretical shapes and experiments.

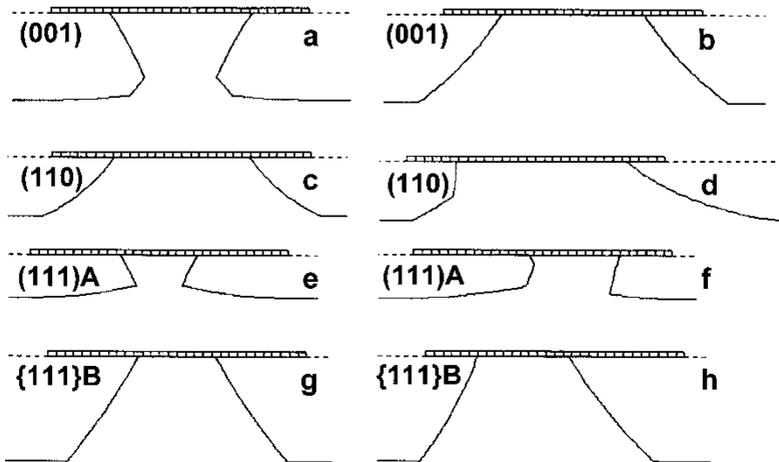


FIGURE 11 Theoretical 2D etching shapes for the cross-sections of grooves etched on surfaces indicated in the figures and aligned along specified directions defined by an angle Ψ_A . Dissolution profiles are derived from law 2. For various surfaces the angle Ψ_A takes the following values: (a) $\Psi_A = +45^\circ$, (b) $\Psi_A = -45^\circ$, (c, e, g) $\Psi_A = 0^\circ$, (d, f, h) $\Psi_A = -90^\circ$. The duration of etching in the case of profiles (c) and (d) is divided by 2.

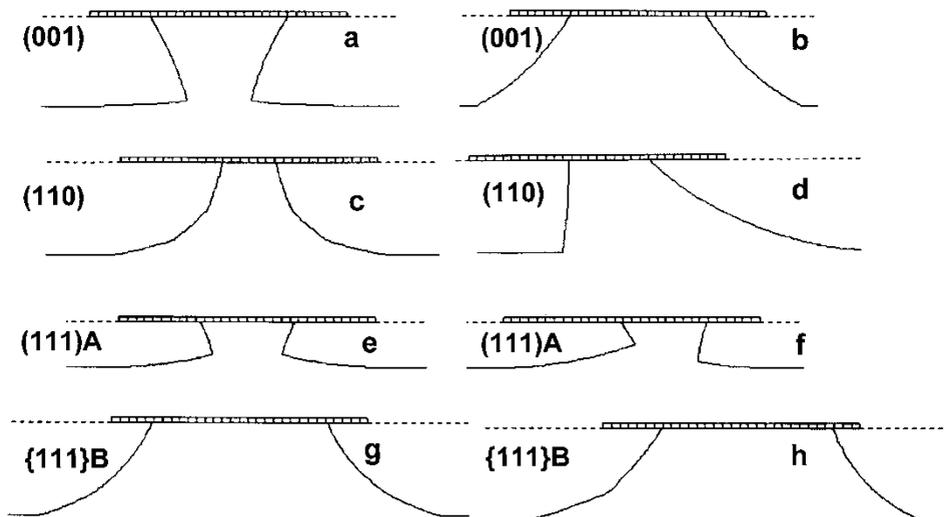


FIGURE 12 Theoretical 2D etching shapes for the cross-sections of grooves etched on surfaces indicated in the figures and aligned along specified directions defined by an angle Ψ_A . Dissolution profiles are derived from law 1. For various surfaces the angle Ψ_A takes the following values: (a) $\Psi_A = +45^\circ$, (b) $\Psi_A = -45^\circ$, (c, e, g) $\Psi_A = 0^\circ$, (d, f, h) $\Psi_A = -90^\circ$. Owing to the anisotropy ratio the duration of etching in the case of profiles (g) and (h) ($\{111\}B$ surface) is divided by 2.

The situation is more complex for $(1\bar{1}0)$ cross-sectional profiles. Cross-sectional etching shapes exhibit two different profiles whatever the law under consideration. The right profile named for convenience profile 2 is exclusively composed of elements with an outward normal. In most cases profile 2 is a curved profile with intersection angle in the range $(50^\circ-10^\circ)$ (see Tab. VI) in close accordance with observations [8] made on (110) substrates etched in the $H_2SO_4:H_2O_2:H_2O$ system. The formation of this curved sidewall is intimately connected with the presence of maxima in the $\{110\}$ polar diagrams (Figs 6 and 7) corresponding to $\{111\}A$ facets. All theoretical profiles 1 (Figs 9d–12d) exhibit a nearly vertical element as frequently observed in literature [8, 9]. Careful examination of $\{110\}$ polar graphs reveals that this element corresponds to the formation of the $\{100\}$ facet for which a maximum of L occurs on polar diagrams. We can also distinguish on some cross-sectional profile 1 a linear element associated with a $\{111\}B$ facet (intersection angle $\alpha_i \approx 35^\circ$) when a second maximum occurs on $\{110\}$ polar diagrams for an orientation corresponding to the $\{111\}B$

TABLE V Values for the Successive Intersection Angles α_i as Measured on the Theoretical Profiles (a, b) of Figures 10–13.

	Surface (001)	
	Section $(1\bar{1}0)$	Section (110)
Law 1	$-61^\circ, 55^\circ$	55°
Law 2	$-61^\circ, 47^\circ$	55°
Law 3	$-60^\circ, 51^\circ$	55°
Law 4	-62°	54°
Observations *	$-60^\circ \sim -75^\circ$	45°
Observations**	$-73^\circ, 60^\circ \sim 10^\circ$	$52^\circ \sim 10^\circ$

Note: (*) and (**) are for experimental values as reported by Iida and Ito for the H_2SO_4 systems (*) and by Takebe *et al.* for HF mixtures (**), respectively.

TABLE VI Values for the Successive Intersection Angles α_i as Measured on the Theoretical Profiles (c, d) of Figures 10–13.

	Surface (110)		
	Section (001)	Section ($\bar{1}\bar{1}0$)	
		Profile 1	Profile 2
Law 1	70°, 40°, 17°	50° ~ 25° ^Y	90°, 50°
Law 2	64° ^Y , 20° ^Y	40° ~ 15° ^Y	90°, 36°
Law 3	50° ~ 30° ^Y	40° ~ 10° ^Y	90°, 30°
Law 4	70°, 40°, 17°	40° ~ 15° ^Y	90°
Observations *	-60° ~ -75°	35° ~ 20°	90° ~ 85°
Observations**	-73°, 60° ~ 10°	35° ~ 8°	88° ~ 37°, 36° ~ 11°

Note: (*) and (**) are for experimental values as reported by Iida and Ito for the H₂SO₄ systems (*) and by Takebe *et al.* for HF mixtures (**), respectively. ^Y indicates the formation of a curved profile.

plane (law 2 for example, Figs 6 and 10d). Takebe *et al.* [9] indicated that HF:H₂O₂:H₂O mixtures result in ($\bar{1}\bar{1}0$) cross-sections where profiles 1 contain two elements, a vertical element and a less-inclined element related to {001} and {111}B facets, respectively. Examination of Table VI gives evidence of an accordance between the theoretical and experimental values of successive intersection angles.

Analysis of theoretical shapes for grooves etched on {111} surfaces shows that the cross-sectional profiles related to the {111}B surface [Figs 9(g,h)–12(g,h)] are relatively “smooth” (more and less curved elements with outward normal) whereas the {111}A cross-sectional profiles are re-entrant profiles [Figs 9(e,f)–12(e,f)]. Let us consider {110} sections etched on the {111}B surface [Figs 9(h)–12(h)]. Elements with α_i values in the range (70°, 55°) and (60°, 58°) compose theoretical profiles 1 and 2 (see Tab. VIII) derived from laws 1, 3 and 4. These values deviate by less than 5% from the values measured for HF:H₂O₂:H₂O and H₂SO₄:H₂O₂:H₂O mixtures [9]. Theoretical values of α_i related to {112} sections [Figs 9(g)–12(g)] are also not far from experimental values for these laws. So theoretical results for the {111}B surface are not very different from the conclusions made by several authors [8, 9]. Examining now theoretical shapes of grooves micromachined on {111}A surfaces it appears [Figs 9(e,f)–12(e,f)] that {112} sections show [Figs 9(e)–12(e)] re-entrant profiles with a mean slope of about -70°. Profile 2 in {110} sections [Figs 9(f)–12(f)] is also re-entrant whereas shapes of profile 1 depend markedly on the etching law. Unfortunately the

TABLE VII Values for the Successive Intersection Angles α_i as Measured on the Theoretical Profiles (c, d) of Figures 10–13.

	Surface (111)		
	Section {112}	Section {110}	
		Profile 1	Profile 2
Law 1	-65°, 75°, 17° ~ 0° ^Y	-85°, 47°, 10° ~ 0° ^Y	-80° ~ 90° ^Y , 10° ~ 0° ^Y
Law 2	-72°, 17° ~ 0° ^Y	-75°, 15° ~ 0° ^Y	-71°, 7° ~ 0° ^Y
Law 3	-65°, 11° ~ 0° ^Y	-61°, 10° ~ 0° ^Y	-67°, 5° ~ 0° ^Y
Law 4	-70°, 17° ~ 0° ^Y	-58°, 18° ~ 0° ^Y	-74°, 5° ~ 0° ^Y
Observations *	-	-	-
Observations**	-	-82° to -68°, 12° ^Y	90° to 13°

Note: (*) and (**) are for experimental values as reported by Iida and Ito for the H₂SO₄ systems (*) and by Takebe *et al.* for HF mixtures (**), respectively. ^Y indicates the formation of a curved profile.

TABLE VIII Values for the Intersection Angles α_i as Measured on the Theoretical Profiles (c, d) of Figures 10–13.

	Surface $(\bar{1}\bar{1}\bar{1})$		
	Section $\{112\}$	Section $\{110\}$	
		Profile 1	Profile 2
Law 1	60°, 16°	65°, 15°	90°, 51°, 15°
Law 2	70°, 44°	70°, 54°	–75° ~ 50° [‡]
Law 3	58°	64°, 60° [‡]	57°, 50° [‡]
Law 4	60° ~ 24° [‡]	68° ~ 30° [‡]	53°, 23°
Observations*	59°	70° – 60°	55° – 50°
Observations**	59°	67° – 9°	–78°, 63° – 9°

Note: (*) and (**) are for experimental values as reported by Iida and Ito for the H₂SO₄ systems (*) and by Takebe *et al.* for HF mixtures (**), respectively. [‡]indicates the formation of a curved profile. The formation of two profile elements close together can be correlated to the development of a slightly curved profile.

absence of experimental values for inclination angles that make cross-sectional profiles related to $\{111\}$ A surfaces does not allow us to proceed with a meaningful discussion.

3.4 Micromachined Structures

It might also be of interest to follow the changes in shape of micromachined membranes and mesa with the geometry of the dissolution slowness surface. Effectively the etching shape of the micromachined structure can be more easily correlated [18–20, 25, 26] to the presence of protuberances and of valleys in the dissolution slowness surface if we start with circular masks. Effectively in this case the simulator works with the whole dissolution slowness because we are concerned with complete 3D etching shapes [18–20]. So in terms of dissolution criteria, facets that bound membranes correspond to peaks of the dissolution slowness surface whereas facets that limit mesa and cause the convex undercutting are connected with valleys [18–20, 25, 28, 29]. Moreover, attempts are made to identify the type of anisotropy (type 1 or type 2) that affect the micromachining of GaAs structures. Let us recall that an anisotropy of type 1 [20] is caused by the presence of very accentuated protuberances in the dissolution slowness surface associated with $\{111\}$ facets and by the simultaneous existence of valleys. So an anisotropy of type 1 results in marked concave and convex undercutting when we micromachine “circular” membranes and mesa, respectively. In contrast an anisotropy of type 2 firstly causes no marked convex undercutting (mesa) and secondly, produces membranes with nearly circular top contour. Anisotropy of type 1 and of type 2 describe behaviors observed for silicon [18–20, 25, 26, 28, 29] and quartz [30] crystals, respectively.

Some theoretical shapes of membranes and mesa etched in (100), (110) and $\{111\}$ surfaces are shown in Figures 13–16. Taking into account the elements of symmetry of GaAs crystal ((100) and (111) directions are $\bar{4}$ and 3 axes, respectively, $\{110\}$ planes are mirror planes) only half-structures are represented in these figures. Several conclusions arise from these figures:

- (i) $\{111\}$ facets limit (001) membranes. One facet possesses an outward normal. The other facet with an inward normal forms a sharp edge (a sharp edge is denoted as SP in the figures or is repaired by a dotted arrow) beneath the mask. This remark remains valid for the four laws, so taking into account the discussion made in Section 3.3 we infer that shoulders of (001) membranes are $\{111\}$ A facets.

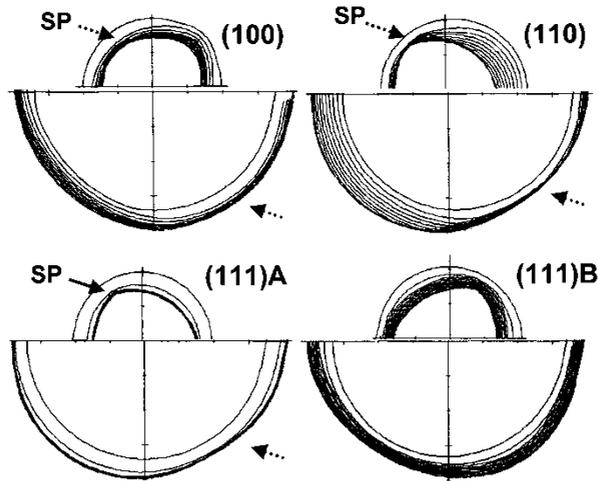


FIGURE 13 Theoretical 3D etching shapes for mesa-membrane structures etched on surfaces indicated in figures. The 3D shapes are derived from the simulator TENSOSIM using law 1 for the database.

- (ii) The convex corner undercutting for (001) mesa depends on the accentuation of minima (valleys) of the dissolution slowness surface. Effectively it is more marked for laws 3 and 4 than for law 1 (compare the polar plots of Figs 6 and 7). Evolution in the shape for (110) and $\{111\}$ mesa calls for a similar remark.
- (iii) If we look at (110) structures we observe for some laws (laws 2 and 3) the development of a supplementary facet (f_s on Fig. 15) that intersects the reference (110) surface along a $\langle 110 \rangle$ direction. So this facet can be identified with a $\{111\}B$ facet because for these two laws a $\{111\}B$ facet is associated with a secondary maximum that can be easily distinguished on the (110) polar diagrams of Figures 6 and 7.
- (iv) The lateral extent of shoulders bordering the $\{111\}B$ mesa and membranes is found to depend strongly on the geometry of the different dissolution slowness surfaces.

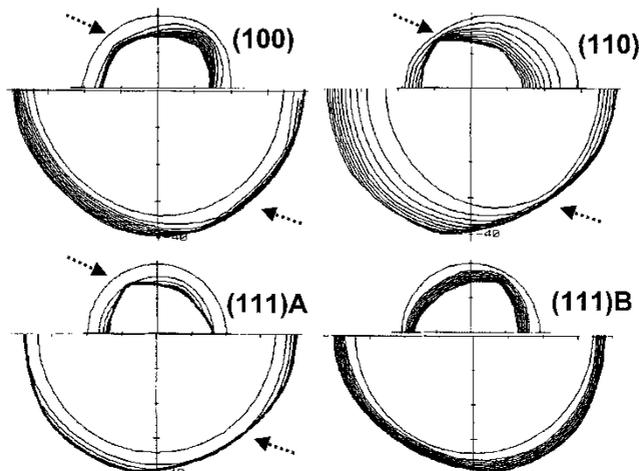


FIGURE 14 Theoretical 3D etching shapes for mesa-membrane structures etched on surfaces indicated in figures. The 3D shapes are derived from the simulator TENSOSIM using law 2 for the database.

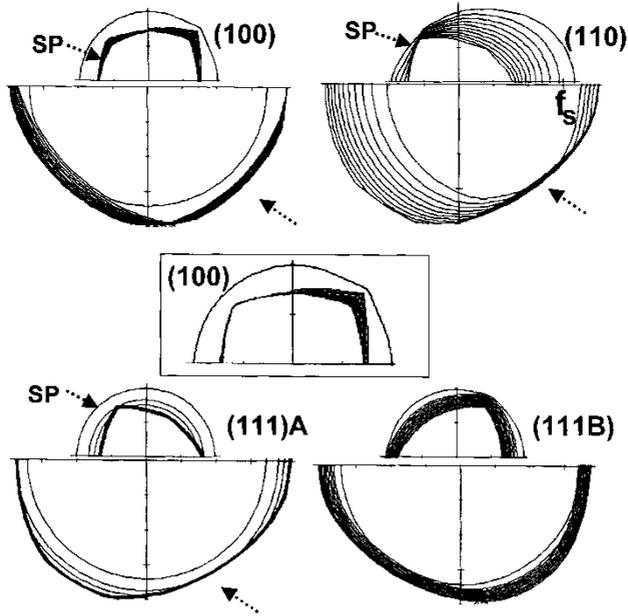


FIGURE 15 Theoretical 3D etching shapes for mesa-membrane structures etched on surfaces indicated in figures. The 3D shapes are derived from the simulator TENSOSIM using law 3 for the database.

- (v) The upper contours of membranes and mesa are not exclusively composed of linear segments in contrast with the behavior observed for such structures micromachined in silicon surfaces. In fact we are concerned either with rounded contours (laws 1 and 4) or with partly rounded contours (laws 2 and 3). So the anisotropy seems to be closer from an anisotropy of type 2 than from an anisotropy of type 1. We regret the absence of published images for structures micromachined in GaAs surfaces that does not allow us to proceed with the discussion.

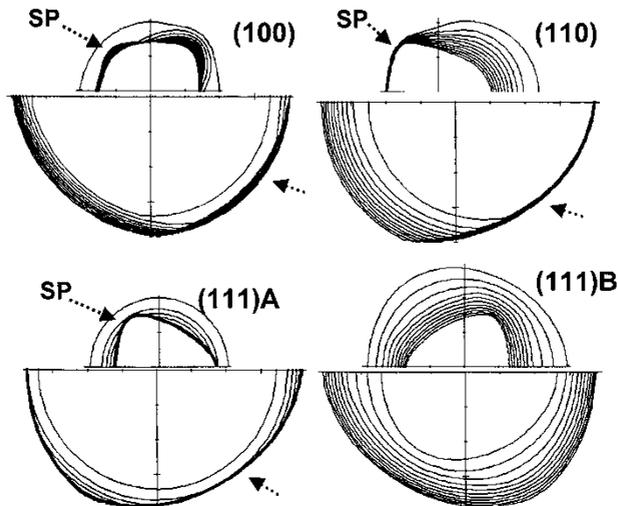


FIGURE 16 Theoretical 3D etching shapes for mesa-membrane structures etched on surfaces indicated in figures. The 3D shapes are derived from the simulator TENSOSIM using law 4 for the database.

4 CONCLUSION

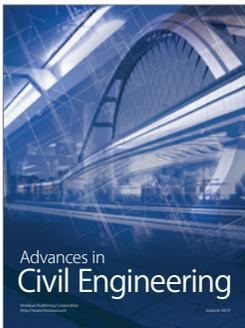
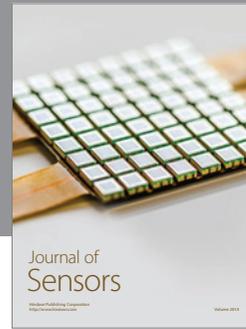
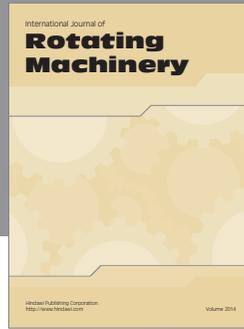
In this paper we propose an analytical equation for the dissolution slowness surface of crystals that belong to the crystallographic class $(\bar{4}3m)$. This equation involves orientation functions that pass through extrema for a limited number of orientations. The main orientations are $\{100\}$, $\{110\}$ and $\{111\}$ surfaces. Several databases composed of dissolution constants are proposed that seem in relative agreement with previous experimental results. The simulator TENSOSIM was used to derive theoretical cross-sectional shapes for grooves aligned along specified directions. It is shown that for (001) grooves it is possible to account for experimental observations by modifying the anisotropy ratio. Moreover for grooves etched in $\{110\}$ and $\{111\}$ surfaces some theoretical results are not far from experiments.

A relatively moderate convex corner undercutting affects mesa as expected for a dissolution process governed by orientation, but for which deviations between amplitudes of successive extrema in the dissolution slowness surface are considerably less marked than for the silicon crystal. It is clear now that to draw final conclusions we have to study experimentally the etching of the GaAs crystal in various etching systems. This relatively long study will be reported in a future paper.

References

- [1] Dario, P., De Rooij, N., Puers, B. and Leistiko, O. (1995). A piezoresistive GaAs pressure sensor with GaAs-AlGaAs membrane technology. *J. Micromech. Microeng.*, **5**, 139–142.
- [2] Hjort, K., Soderkvist, J. and Schweitz, J. A. (1994). Gallium arsenide as a mechanical material. *J. Micromech. Microeng.*, **4**, 1–13.
- [3] Fricke, K. (1991). Piezoelectric properties of GaAs for application in stress transducers. *J. Appl. Phys.*, **70**, 914–918.
- [4] Soderkvist, J. and Hjort, K. (1994). The piezoelectric effect of GaAs used for resonators and resonant sensors. *J. Micromech. Microeng.*, **4**, 28–34.
- [5] Hsu, Y. W., Wang, W. L., Ding, P. D., Liao, K. J. and Wang, J. (1999). Piezoresistive response induced by piezoelectric charges in n-type GaAs mesa resistors for application in stress transducers. *J. Appl. Phys.*, **86**, 5185–5193.
- [6] Schweeger, G., Lang, C., Fricke, K., Hartnagel, H. L., Dolt, R. and Hohenberg, G. (1994). Active GaAs sensor element for dynamic pressure measurements. *Electron. Lett.*, **30**, 1355–1356.
- [7] Shaw, D. W. (1981). Localized GaAs etching with acidic hydrogen peroxide solutions. *J. Electrochem. Soc. Solid State Science and Technology*, **128**, 874–880.
- [8] Iida, S. and Ito, K. (1971). Selective etching of gallium arsenide crystals in $H_2SO_4-H_2O_2-H_2O$ system. *J. Electrochem. Soc. Solid State Science*, **118**, 768–771.
- [9] Takebe, T., Yamamoto, T., Fujii, M. and Kobayashi, K. (1993). Fundamental selective etching characteristics of $HF + H_2O_2 + H_2O$ mixtures for GaAs. *J. Electrochem. Soc.*, **140**, 1169–1180.
- [10] Mori, Y. and Watanabe, N. (1978). A new etching solution system, $H_3PO_4-H_2O_2-H_2O$, for GaAs and its kinetics. *J. Electrochem. Soc. Solid State Science and Technology*, **125**, 1510–1514.
- [11] Yoon, H. J., Choi, M. H. and Park, I. S. (1992). The study of native oxide on chemically (100) surfaces. *J. Electrochem. Soc.*, **139**, 3229–3234.
- [12] Desalvo, G. C., Tseng, W. F. and Comas, J. (1992). Etch rates and selectivities of citric acid/hydrogen peroxide on GaAs, $Al_{0.3}Ga_{0.7}As$, $In_{0.2}Ga_{0.8}As$, $In_{0.53}Ga_{0.47}As$, $In_{0.52}Al_{0.48}As$ and InP. *J. Electrochem. Soc.*, **139**, 831–835.
- [13] Sangwall, K. K. (1987). *Etching of Crystals*. North-Holland, Amsterdam.
- [14] Yamaguchi, K. and Tada, S. (1996). Fabrication of GaAs micro-tips for scanning tunneling microscopy by wet etching. *J. Electrochem. Soc. Solid State Science and Technology*, **143**, 2616–2619.
- [15] Tellier, C. R. (1989). A three-dimensional kinematic model for the dissolution of crystals. *J. Cryst. Growth*, **96**, 450–452.
- [16] Tellier, C. R. (1988). Micro-usinage Chimique du Quartz : Modélisation et Contrôle par Microscopie Electronique à Balayage. *Rapport DRET, Convention 85.34.099.470.75.01*, pp. 169.
- [17] Tellier, C. R., Amaudrut, J. Y. and Brahim-Bounab, A. (1991). The dissolution slowness of cubic crystals. Part II. Applications to class 23 and to combined etching and lithography techniques. *J. Mater. Sci.*, **26**, 5595–5607.
- [18] Tellier, C. R. (1998). Anisotropic etching of silicon crystals in KOH solution. Part III. Experimental and theoretical shapes for 3D structures micromachined in (hk0) plates. *J. Mater. Sci.*, **33**, 117–131.

- [19] Tellier, C. R., Charbonnieras, A. A. and Hodebourg, C. (2001). Simulation of etching shapes for {hhl} structures micromachined in a TMAH 25% solution. *Sensor 2001*, May 8–10, 2001, Nuremberg, Germany (AMA Service GmbH Publisher, 2001) pp. 269–274.
- [20] Tellier, C. R. and Charbonnieras, A. R. (2003). Characterisation of the anisotropic chemical attack of (hhl) silicon plates in a TMAH 25 wt% solution: micromachining and adequacy of the dissolution slowness surface. *Sensors and Actuators A*, **105**, 62–75.
- [21] Frank, F. C. (1965). *Growth and Perfection of Crystals*, In: Doremus, R. H., Robert, B. W., Turnbull, D. (Eds.), Wiley, New York, pp. 411–417.
- [22] Van Veenendaal, E., Sato, K., Shikida, M. and Van Suchtelen, J. (2001). Micromorphology of single crystalline silicon surfaces during anisotropic wet etching in KOH and TMAH. *Sensors and Actuators A*, **93**, 219–231.
- [23] (1978). *IEEE Standards on Piezoelectricity*, IEEE, New York, pp. 15.
- [24] Hodebourg, C. and Tellier, C. R. (2001). Some investigations on the anisotropy of the chemical etching of (hk0) and (hhl) silicon plates in a NaOH 35% solution. Part I: 2D etching shapes. *Active and Passive Electronic Components*, **24**, 31–56.
- [25] Tellier, C. R., Hodebourg, C. and Durand S. (2001). Some investigations on the anisotropy of the chemical etching of (hk0) and (hhl) silicon plates in a NaOH 35% solution. Part II: 3D etching shapes, analysis and comparison with KOH 56%. *Active and Passive Electronic Components*, **24**, 243–264.
- [26] Zubel, I. and Barycka, I. (1998). Silicon anisotropic etching in alkaline solutions I. The geometric description of figures developed under etching Si(100) in various solutions. *Sensors and Actuators A*, **70**, 250–259.
- [27] Irving, B. A. (1962). *The Electrochemistry of semiconductors*. In: Holmes, P. J. (Ed.), Academic press, London, pp. 262–294.
- [28] Tellier, C. R., Hodebourg, C. and Leblois, T. G. (2003). Some investigations on the anisotropy of the chemical etching of (hk0) and (hhl) silicon plates in a NaOH 35% solution. Part III: determination of a database for the simulator TENSOSIM and prediction of 2D etching shapes. *Active and Passive Electronic Components*.(to be published).
- [29] Wu, X.-P. and Ko, W. H. (1989). Compensating corner undercutting in anisotropic etching of (100) silicon. *Sensors and Actuators*, **18**, 207–215.
- [30] Tellier, C. R., Messaoudi, T., Leblois, T. G. and Durand, S. (1997). Convex and concave undercutting in the micromachining of quartz and silicon mechanical structures. *11th European Frequency and Time Forum*, March 8–11, 1997, Neufchatel, Switzerland (FSRM Publisher, Neuchâtel), pp. 386–390.



Hindawi

Submit your manuscripts at
<http://www.hindawi.com>

